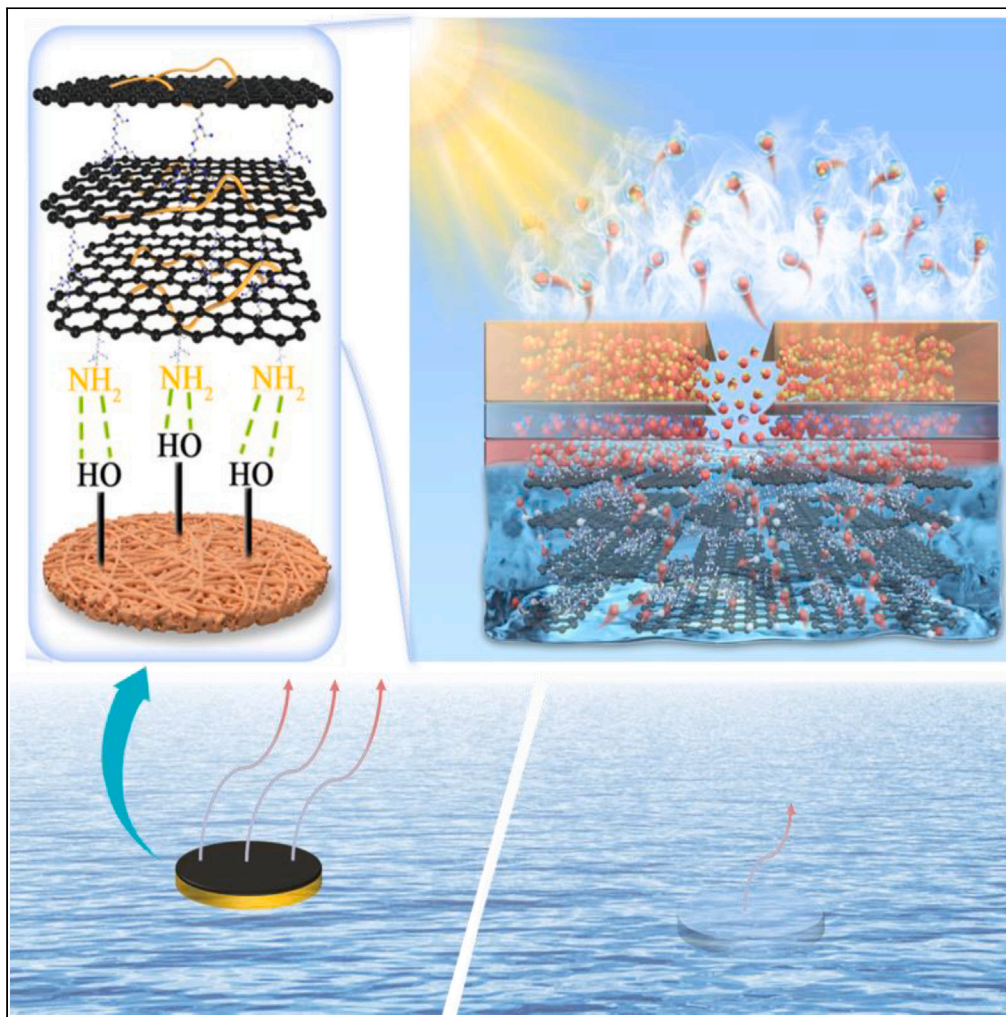


## Article

## A high-efficient and salt-rejecting 2D film for photothermal evaporation



Yiru Su, Lang Liu,  
Xuechao Gao, Wei  
Yu, Ye Hong, Chao  
Liu

l.liu@cqu.edu.cn (L.L.)  
hongye@ciae.ac.cn (Y.H.)

**Highlights**

Tuning thermodynamic states of water molecules to reduce the vaporization enthalpy

Achieving an evaporation rate of 2.48 kg/(m<sup>2</sup>h), exceeding the thermodynamic limit

Cross-linked PEI enables GO membrane to efficiently treat 20 wt % NaCl solution

## Article

A high-efficient and salt-rejecting  
2D film for photothermal evaporationYiru Su,<sup>1</sup> Lang Liu,<sup>1,4,\*</sup> Xuechao Gao,<sup>2</sup> Wei Yu,<sup>1</sup> Ye Hong,<sup>3,\*</sup> and Chao Liu<sup>1</sup>

## SUMMARY

The solar-driven desalination is seen as a sustainable way to combat water scarcity. However, the solar steam generation efficiency has long been restricted by the high vaporization enthalpy of water and low energy density of natural sunlight. We introduced graphene oxide (GO) cross-linked with polyethyleneimine (PEI) as the photothermal material, with the enriched ammonic functional groups in modified GO membrane (GPM) activating water molecules to evaporate with much lower energy consumption. The vaporization enthalpy at the air-film interface is reduced up to 42% in GPM film by tuning the thermodynamic states of water. Consequently, GPM film enables a high evaporation rate of  $2.48 \text{ kg m}^{-2} \text{ h}^{-1}$  with 95.7% energy conversion efficiency under 1 sun. With the aid of positive charges introduced by hydrolysis of PEI, the GPM exhibits excellent salt resistance and delivers an evaporation rate around  $1.8 \text{ kg m}^{-2} \text{ h}^{-1}$  when treating 20 wt % NaCl solution.

## INTRODUCTION

Water security is a serious problem facing the development of whole human society, which has attracted great attention on finding clean and efficient desalination methods. Since membrane separation and thermal distillation are highly energy demanding, interfacial solar steam generator that utilizes solar energy to generate water steam becomes a promising alternative. Recently, intensive endeavors have been made on four aspects to improve the solar steam generation efficiency, such as enhancing sunlight absorption<sup>1–4</sup> and accelerating water transportation<sup>5–7</sup> and reconfiguring the system to improve the thermal management<sup>6,8</sup> and inhibit salt crystallization<sup>9–13</sup> on the photothermal surface. These methods have been proved to enhance the evaporation rate to a certain extent, but all suffering the thermodynamic restriction, i.e., the water vaporization enthalpy is as high as around 2,400 kJ/kg while the energy density of natural sunlight being only about  $1 \text{ kW}/(\text{m}^2 \text{ h})$ .<sup>14</sup> Thereby, a new strategy is addressed in this work to reduce the evaporation enthalpy of water molecules at the air-film interface.<sup>15–17</sup>

Graphene oxide (GO) has strong sunlight absorbance in a wide spectral range,<sup>18,19</sup> while its two-dimensional channel facilitates the transmission of water molecules.<sup>20</sup> Nevertheless, graphene oxide film has a low dimensional stability due to the hydrogen bondings between oxygen-containing functional groups of GO nanosheets, which can be easily destructed by the solution hydration effect. Especially when soaking in salt solution and encountering salt ions, the d-spacing of GO layers is destroyed by size effect.<sup>21</sup> Lim et al.<sup>22</sup> prepared a GO cross-linked membrane with polyethyleneimine (PEI) basing on the principle that catechol group in tannic acid (TA) can react with amine group through Michael addition and/or Schiff base reaction under alkaline conditions, which effectively improved the dimensional stability of the cross-linked layers. Therefore, PEI, possessing rich amino groups, can interact with the carboxylic acid groups with GO nanosheets by forming amide bonds to enhance the structural stability between GO layers. Thanks to its rich amino groups, it also provides the possibility to reduce the evaporation enthalpy, which has been demonstrated in this work. In addition to that, PEI also has the characteristics of polycation, which can be used to provide positive charges on the GO surface, prompting the salt resistance.<sup>23</sup>

Herein, we report an efficient interfacial solar steam generator with the modified GO film delivering greatly reduced vaporization enthalpy to facilitate solar steam generation. As a result, a high evaporation rate of  $2.48 \text{ kg m}^{-2} \text{ h}^{-1}$  was achieved under 1 sun radiation in our fabricated GO-PEI membrane (GPM), achieving a super high solar-to-vapor efficiency of 95.7%. Through testing and theoretical analysis, the evaporation enthalpy in the GPM film is achieved as 1,390 kJ/kg, which is only 58% of the theoretical evaporation

<sup>1</sup>Key Laboratory of Low-Grade Energy Utilization Technologies and Systems, Ministry of Education, School of Energy and Power Engineering, Chongqing University, Chongqing 400044, China

<sup>2</sup>State Key Laboratory of Materials-Oriented Chemical Engineering, College of Chemical Engineering, Nanjing Tech University, 30 Puzhu Road(S), Nanjing 210009, China

<sup>3</sup>Department of Radiochemistry, China Institute of Atomic Energy, Beijing 102413, China

<sup>4</sup>Lead contact

\*Correspondence:  
l.liu@cqu.edu.cn (L.L.),  
hongye@ciae.ac.cn (Y.H.)

<https://doi.org/10.1016/j.isci.2023.107347>



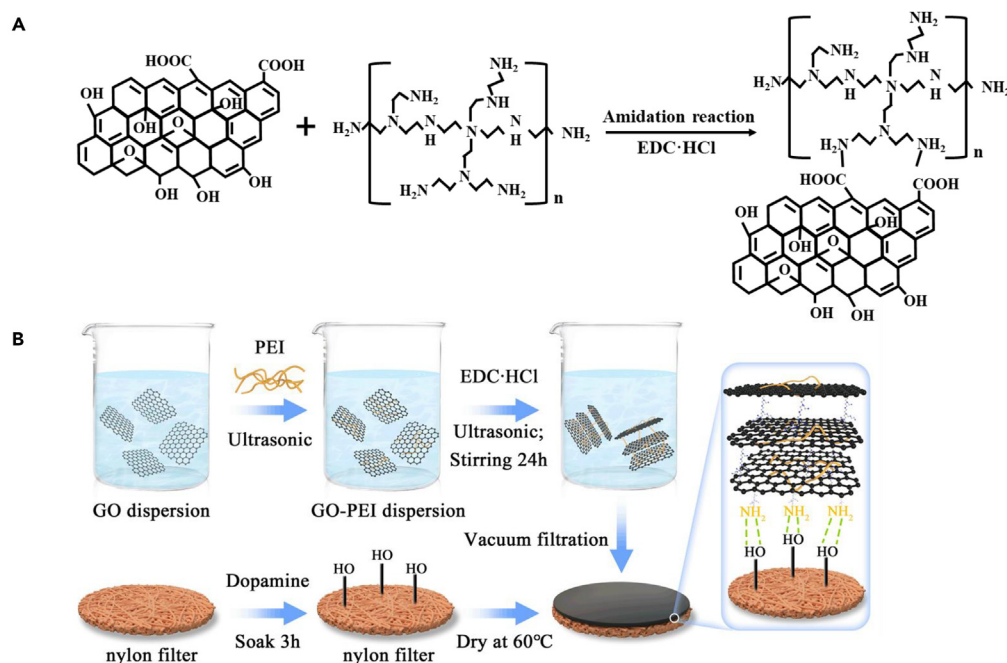


**Figure 1. Preparation of GPMs**

(A) Schematic illustration of the GO cross-linking process with PEI.

(B) Schematic illustration of the preparation process of GPM.

enthalpy of bulk water. In addition, we find our GPM membrane has excellent salt resistance and can maintain efficient and stable evaporation after treating standard seawater for 10 cycles.

## RESULTS AND DISCUSSION

A critical drawback of GO is their low dimensional stability, due to the hydrogen bondings between oxygen-containing functional groups of GO nanosheets, which can be easily destroyed by the aqueous solution hydration effect.<sup>24,25</sup> Therefore, GO is cross-linked with PEI to enhance the membrane dimensional stability when used in desalination. GPMs can be prepared by vacuum filtration and cross-linked with PEI using two-steps method: (1) activating of carboxyl groups of GO and (2) cross-linking with PEI. The GPMs carry high positive charges which could reject positive ions through the Coulomb interactions. A flowchart of fabrication of GPMs is given in Figure 1.

### Characterizations of GPMs

The mass ratio between GO and PEI was tuned to control pore density of cross-linked membrane. GPMs with GO/PEI mass ratios of 1:20, 1:30, 1:40, and 1:50 were prepared (designed as GPM1, GPM2, GPM3, and GPM4, respectively). The Fourier transform infrared (FTIR) spectroscopy spectra analysis was used to detect the presence of functional groups on the surface of GO and GPMs, and the results are recorded in Figure 2A for GO and GPM3. The FTIR of GO shows the presence of C-O bond in the alkoxy groups (around  $1,060\text{ cm}^{-1}$ ), C-O bond in the epoxy groups ( $1,227\text{ cm}^{-1}$ ), unoxidized C-C bond of carbonyl group ( $1,620\text{ cm}^{-1}$ ), and carboxyl groups ( $1,733\text{ cm}^{-1}$ ). However, these absorption characteristic peaks disappeared after cross-linking with PEI. Thus, FTIR results of GPM3 indicate that after cross-linking, two new absorption peaks are obtained at  $2,835$  and  $2,940\text{ cm}^{-1}$ , which are assignable to the symmetric and asymmetric stretching modes of methylene ( $-\text{CH}_2$ ) groups in the PEI polymer. In addition, the presence of carbon and nitrogen bonds as the result of the bonded carboxyl groups in GPM3 (peaks at  $1,363$  and  $1,630\text{ cm}^{-1}$ ) can also be observed.<sup>22,26,27</sup> Meanwhile, the peak at  $\sim 1,630\text{ cm}^{-1}$  obtained owing to the characteristic stretching vibration of  $\text{O}=\text{C}-\text{NH}$  groups was observed in GO-PEI spectra, indicating successful covalent binding of PEI. Further, the peak at  $1,431\text{ cm}^{-1}$  shows the presence of C-OH groups.

The surface and cross section scanning electron microscopy (SEM) images of GPM1 and GPM3 are shown in Figures 2B–2E, respectively. (SEM and cross section of four GPMs are placed in Figure S1.) As shown in

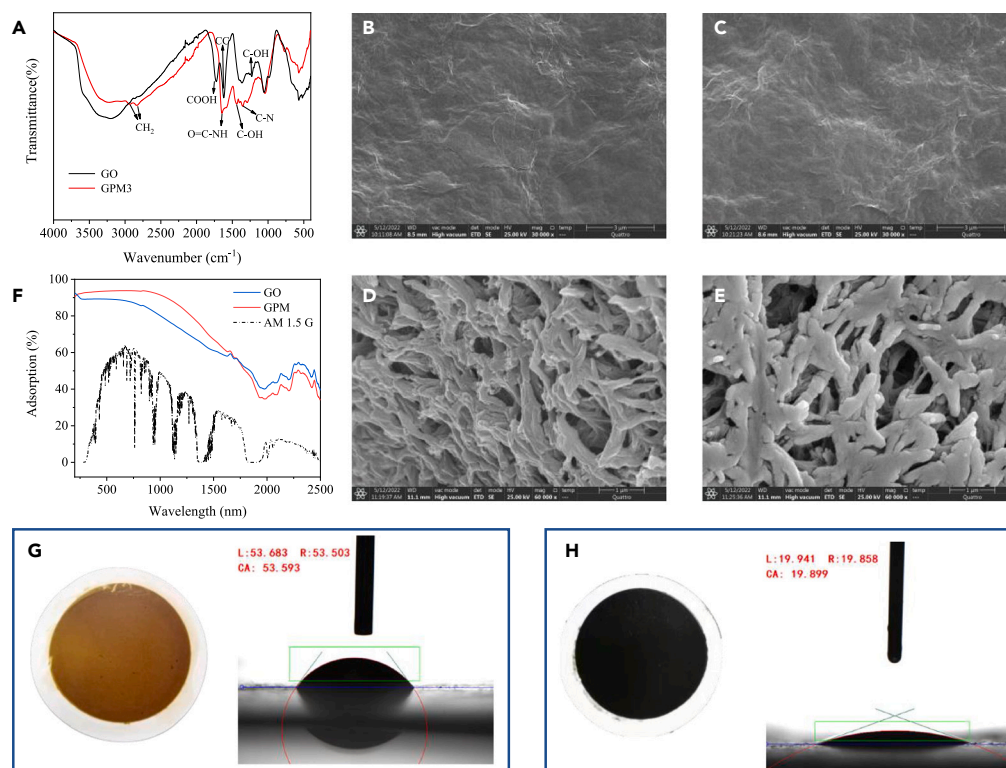


**Figure 2. Characterization of the GPMs**

(A) FTIR spectra of GO and cross-linked GPM3.  
(B and D) Surface and cross section SEM images of GPM1.  
(C and E) Surface and cross section SEM images of GPM3.  
(F) UV-vis NIR spectra of GO and GPM.  
(G and H) Prepared GO and GPM3 films and their water contact angles.

Figures 2B and 2C, the surface of GPMs has typical wrinkled morphology; this corresponds to the multilayer structure of GO, which can enhance the light absorption for existing multi-scattering between layers. Meanwhile, from the scanning diagram of the cross section, there are a lot of pores in the GPM, which is because the presence of PEI, as the cross-linking agent of GO, strengthens the connection between GO layers at the same time. Compared with Figures 2D and 2E, it can be found that with the increase of PEI content, the enlarged porosity is achieved. The enhanced porosity not only strengthens the light absorption performance but also enhances water absorbing.<sup>28</sup> In order to verify this performance, the light absorption of the film and the contact angle of water were tested.

As shown by the ultraviolet-visible (UV-vis) near-infrared (NIR) spectra in Figure 2F, the optical absorption of GPM is stronger than that of GO in the range of ultraviolet and visible light. At the same time, it is clear to see that the color of GPM is darker because after modification the amino groups of PEI are cross-linked with the oxygen-containing functional groups of GO, which is equivalent to the reduction of GO. By testing the contact angle of water, it is found that the contact angle of GPMs (Figure 2H) is smaller than that of GO (Figure 2G) and reduces with the content of PEI, indicating that the hydrophilicity of the cross-linked membrane is enhanced in the GPMs with higher concentration of PEI. The enhanced hydrophilicity is conducive to achieving the balance between water supply and evaporation at the air-film interface so that the membrane surface will not be continuously heated by sunlight due to insufficient water supply, avoiding suffering from excessive surface temperature. Too high surface temperature will not only increase heat loss but also causes irreversible impact on the performance of membrane.

### Solar vapor generation performance

The evaporation device was configured as Figure 3A, in which polyurethane (PU) sponge was adopted to transfer bulk water from bottom to the evaporator surface. Photothermal layer is put on the top of the PU sponge as

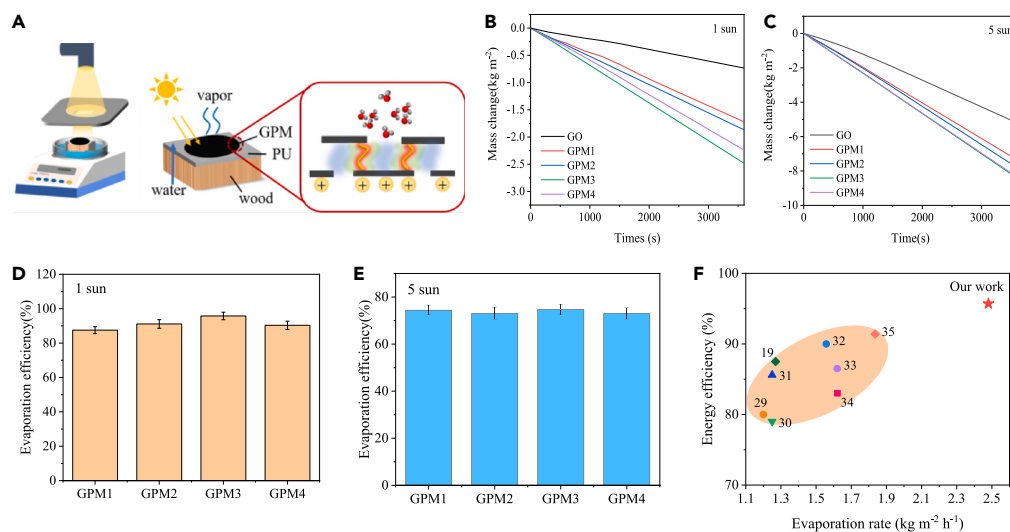


**Figure 3. Schematic diagrams and water evaporation performance**

(A) Evaporation device diagram.

(B) Mass change as a function of time under one sun.

(C) Mass change as a function of time under five sun.

(D) Evaporation efficiencies under one sun.

(E) Evaporation efficiencies under five sun.

(F) Efficiencies versus evaporation rates chart containing the points of our work (star symbol) and other references. These listed data are obtained under the illumination of one sun ( $\sim 1 \text{ kW/m}^2$ ).

light absorber, and wood substrate is placed below PU to be an excellent thermal insulation layer between the photothermal layer and bulk water. A solar light simulator (CEL-HXF300-T3, CEALIGHT) with an optical filter was adopted to produce the simulated sunlight with the standard air mass (AM) 1.5G solar spectrum.

Under one sun (energy density of  $\sim 1 \text{ kW/m}^2$ ) illumination, the surface of GO and GPMs reached stable temperatures around  $46^\circ\text{C}$  within 20 min, illustrated in Figure S2. This indicates that both GO and GPMs as light absorbers have fast thermal response and excellent photothermal conversion ability. Meanwhile, under five sun, GO and GPMs reached a steady surface temperature around  $64^\circ\text{C}$  in almost 5 min. Thanks to the good water transport ability of the membrane themselves, the temperature of the membrane surface can still maintain an acceptable temperature.

The measured evaporation performances of GO and GPMs under 1 sun and 5 sun are illustrated in Figures 3B and 3C. The evaporation rates of GPMs are much higher than those of GO membrane, with GPM3 achieving the best performance among four cross-linked membranes, both under 1 sun and 5 sun illuminations. In particular, the evaporation rate of GPM3 under one sunlight reached  $2.48 \text{ kg m}^{-2} \text{ h}^{-1}$ , exceeding the limit of thermodynamics ( $1.48 \text{ kg m}^{-2} \text{ h}^{-1}$ , given that  $h_{\text{vap}} = 2400 \text{ kJ/kg}$ ). This result is unprecedentedly as high as 337%, 144%, 125%, and 110% of the corresponding evaporation rate in GO, GPM1, GPM2, and GPM4. On the other hand, the evaporation efficiency of GPMs is shown in Figures 3D and 3E. It can be seen the evaporation efficiency of GPM3 reached up to 95.7% under 1 sun. See Supplementary Information (SI) for the detailed information of the calculation of evaporation efficiency. As illustrated in Figure 3F, both the evaporation rate and thermal efficiency in GPM3 are higher than those in most of reported state-of-the-art systems. In addition, to the best of our knowledge, this is the highest evaporation rate reported for two-dimensional membrane evaporators.

### Mechanism for high solar steam generation efficiency

At the photothermal interface, water molecules are initially heated by the solar energy converted and conducted by the GO films and then breaking hydrogen bonds networks to escape from the surface into air. If the energy required for a water molecule to break the hydrogen bond networks could be reduced, the vaporization enthalpy should be reduced accordingly so that more water molecules can escape from the evaporation surface under a fixed sunlight intensity. Thereby, we introduced PEI as the adhesive into

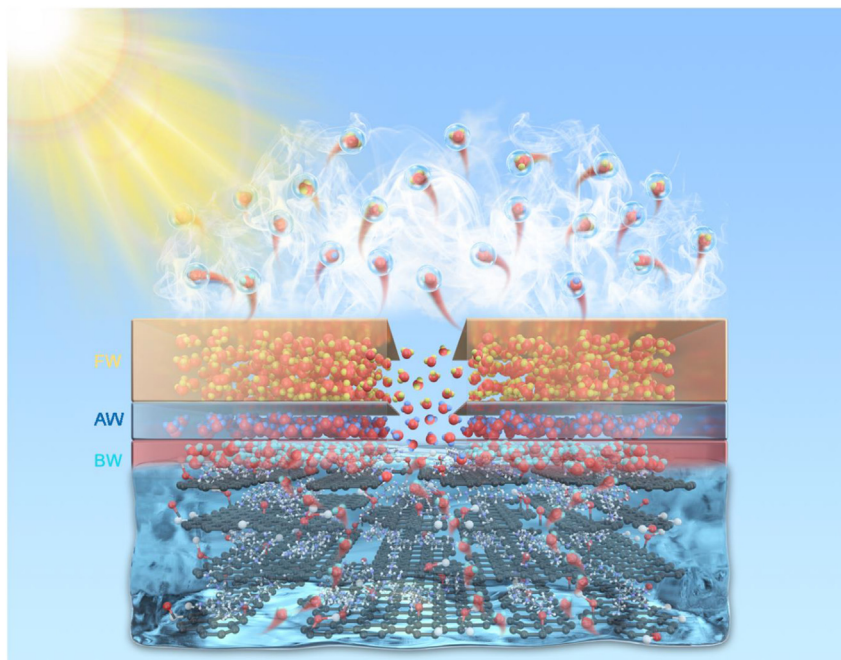


**Figure 4. Schematic diagram of water evaporation on the GPM surface, with water molecules exhibiting different thermodynamic states at the interface**

lamella GO layers and used its enriched  $\text{NH}_2$  groups to activate water molecules into a metastable state, which are quite responsive to the energy input from GPMs surface. The presence of enriched  $\text{NH}_2$  groups will first attract water molecules to form strong covalent bondings with them, and those covalently bonding water (BW) molecules are extremely energy demanding to break the bonding networks for evaporation. Nevertheless, anchored BW molecules could trap some water molecules to tend to divorce from free water (FW) molecules, those having normal hydrogen bonding networks, while not being able to completely pull them off to bond with themselves. These activated water (AW) molecules undergoing the trapping forces from both BW and FW molecules must stay in a metastable state, bearing weakened bonding connections either with BW or with FW molecules. AW molecules need much less energy to break its connection networks when evaporating at the GPM surface. Therefore, it is intuitively anticipated that enhancing the proportion of AW molecules will dramatically reduce the vaporization enthalpy.<sup>17</sup> For visualization, Figure 4 depicts the different states of water molecules at the evaporation surface of GPMs.

In order to prove that there are different states of water molecules on the membrane surface and in between the GO layers, we measured the Raman spectra of water molecules on the surface of GPMs. The peaks measured by Raman spectroscopy contain two modes<sup>17,29</sup>: (1) water molecules with four hydrogen bonds, i.e., two proton and two electron pairs, are involved in hydrogen bonding (the peaks at 3,233 and 3,401  $\text{cm}^{-1}$ ), referring to FW and BW and (2) weakly or non-hydrogen-bonded water molecules in which the hydrogen bonds of the water molecules have been broken, in part or entirely (the peaks at 3,514 and 3,630  $\text{cm}^{-1}$ ), referring AW. Since the proportion of BW should be much smaller than that of FW and it can hardly evaporate at the surface, the ratio of AW:FW is simply standing for the ratio of AW:(FW + BW). As shown in Figure 5, the AW:FW ratios of GPMs are 0.78:1 (Figure 5A), 0.816:1 (Figure 5B), 0.85:1 (Figure 5C), and 0.79:1 (Figure 5D) respectively. Note that the Raman spectroscopy detects the ratio of AW:FW in the whole GPMs samples, with AW molecules tending to exist at the evaporation surface for the less confined space. Therefore, the real differences in the ratios of AW:FW at the evaporation surface should be enlarged compared to the results detected by Raman spectroscopy. The proportion of AW:FW of GPM3 is the highest among the GPMs detected, accounting for the lowest evaporation enthalpy associated with the highest evaporation rate under 1 sun.

It is clearly shown that the significant increase of evaporation rates in GPMs compared to GO is attributed to the reduction in evaporation enthalpy. A dark-condition experiment was conducted to evaluate the

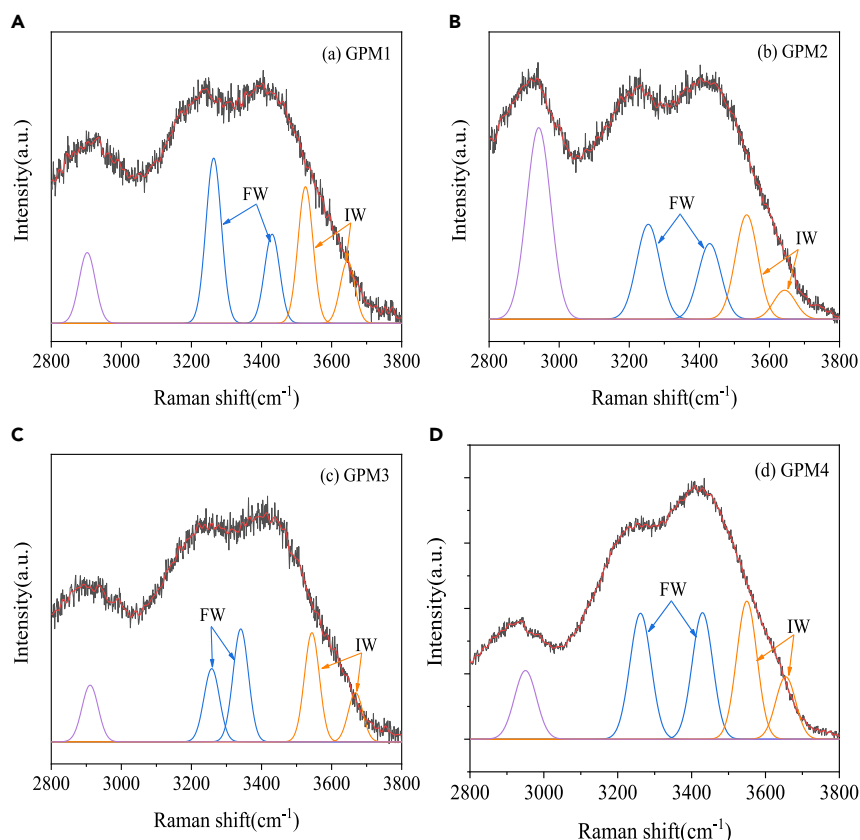


**Figure 5. Fitting curves in the energy region of O-H stretching modes**  
(A–D) Ratio of AW to FW on GPM1(A), GPM2 (B), GPM3 (C), GPM4 (D).

vaporization enthalpy of water at the GO and GPMs surfaces, with the calculated evaporation enthalpies being listed in Tables 1 and S1. It is surprisingly seen that the vaporization enthalpies are reduced to almost half of the standard value of pure water. Additionally, differential scanning calorimetry (DSC) experiments were conducted to further support our evaluations. Detailed descriptions about the vaporization enthalpy measurements are presented in Methods section and SI. To further illustrate the role of AW and FW on determining the evaporation efficiency, the comparison between the evaporation rates of pure water and water absorbed in GPMs under the same light density was tested, with the detailed results given in Figure S5. It is known that water molecules in pure water mainly exist in the form of FW, while on the surface of GPMs, they exist in the form of AW-FW distribution. Under one sunlight, the evaporation rate of pure water is detected as  $0.228 \text{ kg m}^{-2} \text{ h}^{-1}$ , which is far lower than that on the surface of GPMs.

However, under the condition of intensified solar density (5 sun), the vaporization enthalpy tuning theory seems invalid to explain the evaporation performance. Theoretically, if the composition of AW and FW is fixed at the photothermal interface, the observed evaporation rate should be increased by 5-folds. Nevertheless, as given in Figures 3C and 3D, the evaporation rates did not increase linearly with sunlight density, which indicates that the composition of water molecules of different states varies when sunlight is intensified. Although the temperature at the interface of GPMs is increased when the solar density is increased from 1 sun to 5 sun, it is believed that the forming rates of AW at the air-film deviate only slightly. Thereby, the contribution from AW to the evaporation rate will be significantly reduced under intensified solar density, as the evaporation occurring through FW molecules will be more prevalent. Due to the enlarged portion of FW molecules evaporating at the surface, the vaporization enthalpy is enhanced accordingly. Meanwhile, in the test of 5 sun, although GPM3 still maintains the best evaporation performance with high AW content, the difference between GPM3 and GPM4 is very small, which is only about 0.77%. In consideration of the enlarged portion of FW evaporating at the interface under 5 sun, the difference between the effective vaporization enthalpies of GPM3 and GPM4 is expected to be negligible, such

**Table 1. Evaporation enthalpies of water in GPMs determined in this work**

1sun-Evaporators	$T_1$ (K)	$h_{water,T_1}$ ( $J g^{-1}$ ) (bulk water)	$h_{eve,T_1}$ ( $J g^{-1}$ ) (in GPMs)
GPM1	316.9	2404	1832
GPM2	318	2401	1562
GPM3	319.8	2396	1390
GPM4	320	2396	1452

that the evaporation rates between these two films are quite similar. However, the enhanced temperature of the GPMs surface under 5 sun leads to enhanced heat loss, which may also be partially accounting for the non-proportional increment in the evaporation rate, evident in [Figure S2](#).

### Solar desalination performance

The desalination performance of the GPMs was tested by treating 3.5 wt % NaCl solution. As shown in [Figure 6A](#), the evaporation rates of the GPM membranes are only slightly reduced, compared to treating pure water. For instance, the evaporation rate in GPM3 only reduces from 2.48 to 2.47  $kg m^{-2} h^{-1}$ . Further, all the GPM membranes can maintain high and stable evaporation rates with no salt crystals deposited on the surface when treating the 3.5 wt % brine after 10 repeated cycles with each cycle lasting for 1 h. In fact, even for the near-saturation brine (20 wt %), evaporation rate can still be maintained at about 1.8  $kg m^{-2} h^{-1}$ , which is higher than most reported results,<sup>19,28,30–35</sup> evident in [Figures 6F](#) and [3F](#).

To further certify the reusability of the GPMs for concentrated brine, we configured NaCl solution with a concentration of 8 wt % and tested the GPM3 for 10 cycles, under 1 sun, and each cycle lasted for more than 4 h. Over each cycle, the GPM3 was cleaned with deionized water, and we repeated the experiment after drying the membrane in the drying oven. The results of the cycle test are shown in [Figure 6B](#). Despite the impacts from environmental factors including the change of temperature and humidity along the operation as well as the increase in salt concentration, the evaporation rate of the membrane has always stayed stable around 2.2  $kg m^{-2} h^{-1}$  in 10 tests, and the micro morphology of the membrane has not changed in the whole cycle, indicating that the evaporation performance of the membrane is almost not affected by the number of cycles.

To test the stability and performance of GPMs in daily life, a 10 h continuous evaporation test was carried out for GPM3 film. [Figures 6C](#) and [6D](#) depict that the evaporation rate is stable and no salt crystallization has been observed on the membrane surface during the continuous 10 h evaporation, when treating the 3.5 wt % and 8 wt % brines. Average evaporation rates through 10 h in the 3.5 wt % and 8 wt % brines are both around 2.3 and 2.33  $kg m^{-2} h^{-1}$ , respectively. Note that the change of temperature and humidity along the day and the increase in salt concentration should be responsible for the fluctuations in the evaporation rates.

To push the limit of our designed GPMs, water purification tests for extremely high concentration brine were conducted ([Figure 6E](#) and [6F](#)). However, a small amount of salt crystallized after 10 h operation, when treating the 12.7 wt % brine, and certain regions of the GPM3 film were covered by salt crystal when treating 20 wt % brine. We find the salt crystals on the surface of GPM3 could reduce the evaporation, which is due to the reduced sunlight absorption and blocked water transport channels at the GPM surface. Nevertheless, the reduction in evaporation rate is mild, which is  $\sim 23.5\%$ .

Since the membrane after cross-linking PEI has positive charges, according to the Donnan exclusion effect, the positive charges carried by GPMs will facilitate repelling of the cations, resulting in high rejection of salt ions. As illustrated in [Figure S7A](#) of SI, even with a great amount of crystals accumulated below the membrane, the crystal on the membrane surface can hardly be observed when treating 12.7 wt % NaCl solution. This further emphasizes the great salt repel ability of GPMs. To effectively evaluate the performance of GPMs purified water, the concentration of ions in the solution was characterized by measuring the conductivities of the feed solution and the collected water steam from 3.5 wt % brine. As shown in [Figure S8](#), the conductivity of the solution before evaporation is 74.6  $mS cm^{-1}$ , and the conductivity of the condensed water is 88  $\mu S cm^{-1}$ . The conductivity decreased nearly 1,000 times before and after evaporation, indicating that positive charges carried by GPMs exert positive effect on solar-driven desalination.

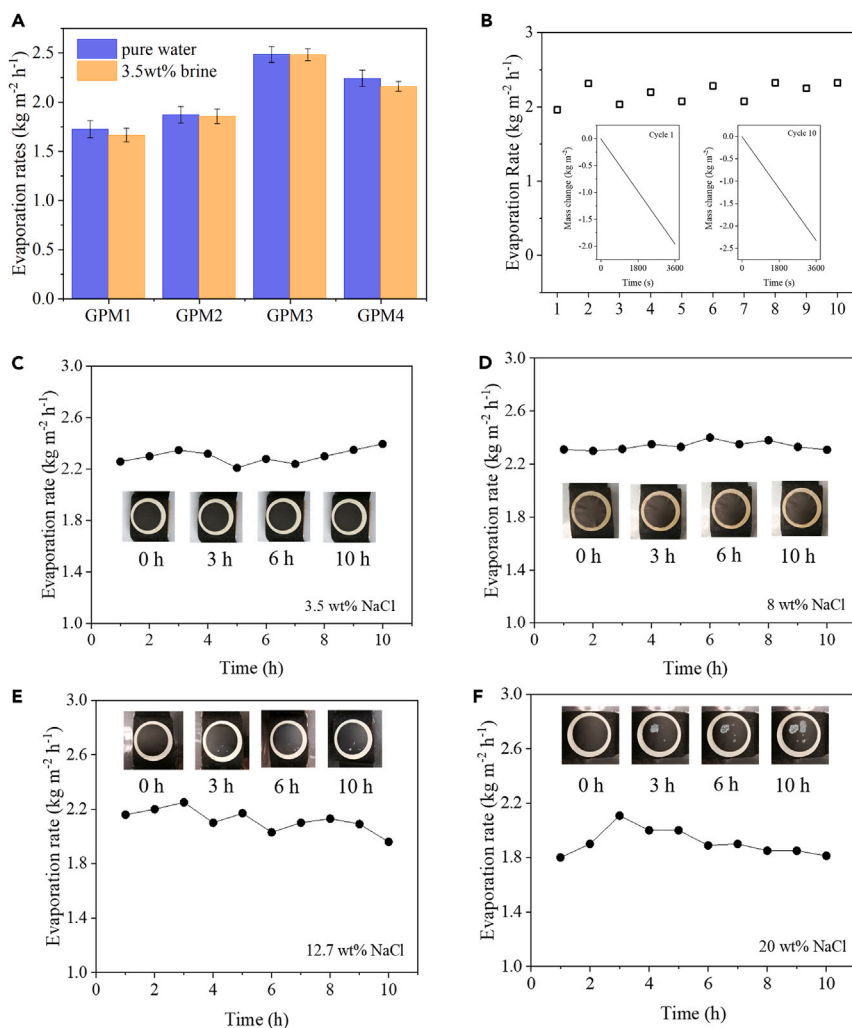


**Figure 6. Desalination performance of GPM3**

(A) Evaporation rates of four GPMs under one sun with 3.5 wt % brine.

(B) The stability test of the GPM3 with 8 wt % NaCl solution over ten cycles. Insets: the mass change of water in the first and tenth cycles.

(C–F) The evaporation rate of the GPM3 in different salinities of NaCl solution. The inset is the photo of surface of the GPM3, in which the crystallization of salt can be observed during the 10-h test.

## Conclusions

This work demonstrated that GO cross-linked with PEI could tune the distribution of water states and subsequently reduces the vaporization enthalpy of water evidently, providing a very promising solution to break the thermodynamic limit of solar-driven desalination. It is found that under 1 sun irradiation, the rate of water evaporation at the air-film interface is mainly contributed by the phase transition of AW molecules, associated with reduced vaporization enthalpy. Because the forming rate of AW in GPM is weakly affected by the solar intensity, the evaporation through the phase transition of FW becomes more prevalent under 5 sun. By adjusting the content of PEI to achieve the lowest vaporization enthalpy of 1,390 kJ/kg, GPM3 enabled a high evaporation rate of 2.48 kg m<sup>-2</sup> h<sup>-1</sup> and the thermal efficiency of 95.7% under 1 sun. In addition, the GPM3 also exhibits excellent stability and durability for treating 3.5 wt % and 12.7 wt % NaCl solutions under 1 sun, thanks to carrying positive charges on the surface of GPMs. Further, even for 20 wt % NaCl, it also shows a high evaporation rate of ~1.8 kg m<sup>-2</sup> h<sup>-1</sup> while having good salt resistance.

**STAR★METHODS**

Detailed methods are provided in the online version of this paper and include the following:

- **KEY RESOURCES TABLE**
- **RESOURCE AVAILABILITY**
  - Lead contact
  - Materials availability
  - Data and code availability
- **METHOD DETAILS**
  - Chemicals and materials
  - Estimation of Effective Vaporization Enthalpy
  - Preparation of GO-PEI membranes
  - Pretreatment of nylon filter membrane
  - Characterizations of the GPMs

**SUPPLEMENTAL INFORMATION**

Supplemental information can be found online at <https://doi.org/10.1016/j.isci.2023.107347>.

**ACKNOWLEDGMENTS**

L. Liu acknowledges National Natural Science Foundation of China (Grant No. 52006017) for the funding support and China Postdoctoral Science Foundation for funding support (2022T150770, 2021M690175).

**AUTHOR CONTRIBUTIONS**

L.L. supervised the project. Y.S. designed the experiments and performed experiments. All authors discussed the experiments and results. Y.S. and L.L. prepared and revised the manuscript.

**DECLARATION OF INTERESTS**

The authors declare that they have no known competing financial interests or personal relationships that could have appeared to influence the work reported in this paper.

The authors declare the following financial interests/personal relationships which may be considered as potential competing interests.

Received: February 9, 2023

Revised: May 27, 2023

Accepted: July 6, 2023

Published: July 13, 2023

**REFERENCES**

1. Li, T., Song, J., Zhao, X., Yang, Z., Pastel, G., Xu, S., Jia, C., Dai, J., Chen, C., Gong, A., et al. (2018). Anisotropic, lightweight, strong, and super thermally insulating nanowood with naturally aligned nanocellulose. *Sci. Adv.* *4*, eaar3724.
2. Wang, X., He, Y., Liu, X., Shi, L., and Zhu, J. (2017). Investigation of photothermal heating enabled by plasmonic nanofluids for direct solar steam generation. *Sol. Energy* *157*, 35–46.
3. Huang, W., Hu, G., Tian, C., Wang, X., Tu, J., Cao, Y., and Zhang, K. (2019). Nature-inspired salt resistant polypyrrole-wood for highly efficient solar steam generation. *Sustain. Energy Fuels* *3*, 3000–3008.
4. Zhou, X., Zhao, F., Guo, Y., Zhang, Y., and Yu, G. (2018). A hydrogel-based antifouling solar evaporator for highly efficient water desalination. *Energy Environ. Sci.* *11*, 1985–1992.
5. Wu, X., Chen, G.Y., Zhang, W., Liu, X., and Xu, H. (2017). A plant-transpiration-process-inspired strategy for highly efficient solar evaporation. *Adv. Sustain. Syst.* *1*, 1700046.
6. Xue, G., Liu, K., Chen, Q., Yang, P., Li, J., Ding, T., Duan, J., Qi, B., and Zhou, J. (2017). Robust and low-cost flame-treated wood for high-performance solar steam generation. *ACS Appl. Mater. Interfaces* *9*, 15052–15057.
7. Li, Y., Alibakhshi, M.A., Zhao, Y., and Duan, C. (2017). Exploring ultimate water capillary evaporation in nanoscale conduits. *Nano Lett.* *17*, 4813–4819.
8. Yin, Z., Wang, H., Jian, M., Li, Y., Xia, K., Zhang, M., Wang, C., Wang, Q., Ma, M., Zheng, Q.S., and Zhang, Y. (2017). Extremely black vertically aligned carbon nanotube arrays for solar steam generation. *ACS Appl. Mater. Interfaces* *9*, 28596–28603.
9. Yang, Y., Zhao, H., Yin, Z., Zhao, J., Yin, X., Li, N., Yin, D., Li, Y., Lei, B., Du, Y., and Que, W. (2018). A general salt-resistant hydrophilic/hydrophobic nanoporous double layer design for efficient and stable solar water evaporation distillation. *Mater. Horiz.* *5*, 1143–1150.
10. Veleva, I., Vanoppen, M., Hitsov, I., Phukan, R., Wyseure, L., Dejaeger, K., Cornelissen, E.R., and Verliefde, A.R.D. (2021). Selection of membranes and operational parameters aiming for the highest rejection of petrochemical pollutants via membrane distillation. *Sep. Purif. Technol.* *259*, 118143.
11. Rad, M.N., Shokri, N., Keshmiri, A., and Withers, P.J. (2015). Effects of grain and pore

- size on salt precipitation during evaporation from porous media. *Transport Porous Media* 110, 281–294.
12. Xu, K., Wang, C., Li, Z., Wu, S., and Wang, J. (2020). Salt mitigation strategies of solar-driven interfacial desalination. *Adv. Funct. Mater.* 31, 2007855.
  13. Chen, J., Yin, J.L., Li, B., Ye, Z., Liu, D., Ding, D., Qian, F., Myung, N.V., Zhang, Q., and Yin, Y. (2020). Janus evaporators with self-recovering hydrophobicity for salt-rejecting interfacial solar desalination. *ACS Nano* 14, 17419–17427.
  14. Song, H., Liu, Y., Liu, Z., Singer, M.H., Li, C., Cheney, A.R., Ji, D., Zhou, L., Zhang, N., Zeng, X., et al. (2018). Cold vapor generation beyond the input solar energy limit. *Adv. Sci.* 5, 1800222.
  15. Yu, Z., Gu, R., Tian, Y., Xie, P., Jin, B., and Cheng, S. (2022). Enhanced interfacial solar evaporation through formation of micro-meniscuses and microdroplets to reduce evaporation enthalpy. *Adv. Funct. Mater.* 32, 2108586.
  16. Guan, Q.F., Han, Z.M., Ling, Z.C., Yang, H.B., and Yu, S.H. (2020). Sustainable wood-based hierarchical solar steam generator: a biomimetic design with reduced vaporization enthalpy of water. *Nano Lett.* 20, 5699–5704.
  17. Zhao, F., Zhou, X., Shi, Y., Qian, X., Alexander, M., Zhao, X., Mendez, S., Yang, R., Qu, L., and Yu, G. (2018). Highly efficient solar vapour generation via hierarchically nanostructured gels. *Nat. Nanotechnol.* 13, 489–495.
  18. Liu, K.K., Jiang, Q., Tadepalli, S., Raliya, R., Biswas, P., Naik, R.R., and Singamaneni, S. (2017). Wood-graphene oxide composite for highly efficient solar steam generation and desalination. *ACS Appl. Mater. Interfaces* 9, 7675–7681.
  19. Li, Y., Gao, T., Yang, Z., Chen, C., Kuang, Y., Song, J., Jia, C., Hitz, E.M., Yang, B., and Hu, L. (2017). Graphene oxide-based evaporator with one-dimensional water transport enabling high-efficiency solar desalination. *Nano Energy* 41, 201–209.
  20. Liu, P.-F., Miao, L., Deng, Z., Zhou, J., Su, H., Sun, L., Tanemura, S., Cao, W., Jiang, F., and Zhao, L.-D. (2018). A mimetic transpiration system for record high conversion efficiency in solar steam generator under one-sun. *Mater. Today Energy* 8, 166–173.
  21. Li, H., Tian, Y., Zhao, X., Mo, Y., and Qi, H. (2021). Competition of co-existing cations to eliminate negative effect of Na<sup>+</sup> on graphene oxide membrane structure and stabilize the separation performance. *Sep. Purif. Technol.* 258, 118020.
  22. Lim, M.-Y., Choi, Y.-S., Kim, J., Kim, K., Shin, H., Kim, J.-J., Shin, D.M., and Lee, J.-C. (2017). Cross-linked graphene oxide membrane having high ion selectivity and antibacterial activity prepared using tannic acid-functionalized graphene oxide and polyethyleneimine. *J. Membr. Sci.* 521, 1–9.
  23. Cai, X., Lin, M., Tan, S., Mai, W., Zhang, Y., Liang, Z., Lin, Z., and Zhang, X. (2012). The use of polyethyleneimine-modified reduced graphene oxide as a substrate for silver nanoparticles to produce a material with lower cytotoxicity and long-term antibacterial activity. *Carbon* 50, 3407–3415.
  24. Kim, S.Y., Cheon, S.Y., Kim, E.J., Lee, J.H., Kam, E.H., Kim, J.M., Park, M., and Koo, B.N. (2017). Highly crosslinked, chlorine tolerant polymer network entwined graphene oxide membrane for water desalination. *Neurochem. Res.* 42, 1533–1542.
  25. Chen, B., Jiang, H., Liu, X., and Hu, X. (2017). Molecular insight into water desalination across multilayer graphene oxide membranes. *ACS Appl. Mater. Interfaces* 9, 22826–22836.
  26. Parsamehr, P.S., Zahed, M., Tofighy, M.A., Mohammadi, T., and Rezakazemi, M. (2019). Preparation of novel cross-linked graphene oxide membrane for desalination applications using (EDC and NHS)-activated graphene oxide and PEI. *Desalination* 468, 114079.
  27. Zhang, Z., Xiao, X., Zhou, Y., Huang, L., Wang, Y., Rong, Q., Han, Z., Qu, H., Zhu, Z., Xu, S., et al. (2021). Bioinspired graphene oxide membranes with pH-responsive nanochannels for high-performance nanofiltration. *ACS Nano* 15, 13178–13187.
  28. Hu, X., Xu, W., Zhou, L., Tan, Y., Wang, Y., Zhu, S., and Zhu, J. (2017). Tailoring graphene oxide-based aerogels for efficient solar steam generation under one sun. *Adv. Mater.* 29, 1604031.
  29. Kudo, K., Ishida, J., Syuu, G., Sekine, Y., and Ikeda-Fukazawa, T. (2014). Structural changes of water in poly(vinyl alcohol) hydrogel during dehydration. *J. Chem. Phys.* 140, 044909.
  30. Li, T., Liu, H., Zhao, X., Chen, G., Dai, J., Pastel, G., Jia, C., Chen, C., Hitz, E., Siddhartha, D., et al. (2018). Scalable and highly efficient mesoporous wood-based solar steam generation device: localized heat, rapid water transport. *Adv. Funct. Mater.* 28, 1707134.
  31. Shi, Y., Zhang, C., Li, R., Zhuo, S., Jin, Y., Shi, L., Hong, S., Chang, J., Ong, C., and Wang, P. (2018). Solar evaporator with controlled salt precipitation for zero liquid discharge desalination. *Environ. Sci. Technol.* 52, 11822–11830.
  32. Li, Y., Gao, T., Yang, Z., Chen, C., Luo, W., Song, J., Hitz, E., Jia, C., Zhou, Y., Liu, B., et al. (2017). 3D-printed, all-in-one evaporator for high-efficiency solar steam generation under 1 sun illumination. *Adv. Mater.* 29, 1700981.
  33. Huo, B., Jiang, D., Cao, X., Liang, H., Liu, Z., Li, C., and Liu, J. (2019). N-doped graphene/carbon hybrid aerogels for efficient solar steam generation. *Carbon* 142, 13–19.
  34. Zhang, P., Li, J., Lv, L., Zhao, Y., and Qu, L. (2017). Vertically aligned graphene sheets membrane for highly efficient solar thermal generation of clean water. *ACS Nano* 11, 5087–5093.
  35. Zhang, H., Xie, H., Han, W., Yan, X., Liu, X., He, L., Lin, P., Xia, Y., Zhang, K., Zapfen, J.A., and Yoon, K.B. (2021). Graphene oxide-reduced graphene oxide Janus membrane for efficient solar generation of water vapor. *ACS Appl. Nano Mater.* 4, 1916–1923.

## STAR★METHODS

## KEY RESOURCES TABLE

REAGENT or RESOURCE	SOURCE	IDENTIFIER
Chemicals, peptides, and recombinant proteins		
Graphene oxide	XFNANO Materials Technology	CAS: 7440-44-0
Tris-hydroxymethyl amino methane	Shanghai Eon Chemical Technology	CAS: 77-86-1
Ethylene imine polymer	Aladdin Biochemecal Technology	CAS: 9002-98-6
N-(3-Dimethylaminopropyl)-N'-ethylcarbodiimide hydrochloride (98%)	Aladdin Biochemecal Technology	CAS: 25952-53-8
dopamine hydrochloride	Aladdin Biochemecal Technology	CAS: 62-31-7
Deposited data		
All data reported in this paper will be shared by the lead contact upon request.		

## RESOURCE AVAILABILITY

## Lead contact

Further inquiries and request for data, strains and resources should be directed to the lead contact Lang Liu [l.liu@cqu.edu.cn](mailto:l.liu@cqu.edu.cn).

## Materials availability

This study did not generate new unique reagents.

## Data and code availability

The published article includes all datasets generated or analyzed during this study.

## METHOD DETAILS

## Chemicals and materials

GO (Product NO: XF002-1) were obtained from XFNANO Materials Technology Co., Ltd, China. Tris-hydroxymethyl amino methane (Tris,  $C_4H_{11}NO_3$ , Mw 121.14 g/mol) was obtained from Shanghai Eon Chemical Technology Co., Ltd, China. Ethylene imine polymer ( $(CH_2CH_2NH)_n$ , Mw 70,000 g/mol), N-(3-Dimethylaminopropyl)-N'-ethylcarbodiimide hydrochloride ( $C_8H_{17}N_3 \cdot HCl$ , Mw 191.7 g/mol), dopamine hydrochloride ( $C_8H_{11}NO_2 \cdot HCl$ , Mw 189.64 g/mol), NaCl ( $\geq 99.5\%$ ) were purchased from Shanghai Aladdin Biochemecal Technology Co., Ltd, China. Organic nylon microporous membrane, from Haiyan New Oriental Plastic Technology Co., Ltd, China, had a nominal pore size of 0.1  $\mu m$ . Deionized (DI) water (electric conductivity  $>18 M\Omega cm$ ) was used to prepare the solution.

## Estimation of Effective Vaporization Enthalpy

In order to obtain the enthalpy of evaporation, we first designed a set of test experiments. The experimental conditions are to select pure water and GPMs of equal area, place them in a closed container, and test the evaporation capacity under dark conditions. Here we assume that the energy input,  $U_{in}$ , of bulk water is the same as that of GPMs, since only the thermal irradiation from environmental is mainly involved. The experiment was conducted in dark under room temperature (25°C) and ambient air pressure with the relative humidity at about 40%. Evaporation rates of bulk water and GPMs are measured and shown in Figure S3A. Subsequently, the corresponding effective evaporation enthalpy ( $\Delta h_{eva,20^\circ C}$ ) of GPMs in the dark condition were calculated following.

$$U_{in} = \Delta h_{water,20^\circ C} \dot{m}_{water,20^\circ C} = \Delta h_{eva,20^\circ C} \dot{m}_{eve,20^\circ C} \quad (\text{Equation 1})$$

where  $\Delta h_{water,20^\circ C}$  and  $\dot{m}_{water,20^\circ C}$  is the evaporation enthalpy and evaporation rate of pure water;  $\dot{m}_{eve,20^\circ C}$  is the evaporation rate of pure water on the GPMs.

Since enthalpy is a state property, so the change in enthalpy is only determined by the initial and final states. Due to the evaporation occurs without reaching its saturation temperature, the evaporation enthalpy of pure water at a temperature  $T_1$  can be virtually determined based on three procedures (1) liquid water is heated to its saturated temperature at the atmospheric pressure, (2) saturated water undergoes the phase change, turning into saturated vapor, (3) saturated vapor cools down to the evaporating temperature  $T_1$ , following the equation

$$h_{\text{water},T_1} = \int_{T_1}^{100^\circ\text{C}} C_{p,l} dT + h_{\text{water},100^\circ\text{C}} + \int_{100^\circ\text{C}}^{T_1} C_{p,g} dT \quad (\text{Equation 2})$$

where  $h_{\text{water},T_1}$  is the evaporation enthalpy of pure water at the temperature  $T_1$  ( $\text{J g}^{-1}$ );  $T_1$  is the steady-temperature of the absorbers and water (K);  $C_{p,l}$  is the heat capacity of the liquid water ( $4.2 \text{ J K}^{-1} \text{ g}^{-1}$ );  $h_{\text{water},100^\circ\text{C}}$  is the evaporation enthalpy (phase transition latent heat) of the water at  $100^\circ\text{C}$  ( $2.257 \text{ MJ kg}^{-1}$ );  $C_{p,g}$  is the heat capacity of water vapor ( $\text{J K}^{-1} \text{ g}^{-1}$ ), and calculated by the following equation:

$$C_{p,g} = (3.470 + 1.45 \times 10^{-3} \times T_1 + 0.121 \times 10^{-5} \times T_1^{-2}) RM^{-1}$$

$R$  is the general gas constant ( $8.314 \text{ J K}^{-1} \text{ mol}^{-1}$ ) and  $M$  is the relative molecular mass of water ( $18.02 \text{ g mol}^{-1}$ ).<sup>2</sup>

Thus, the evaporation enthalpy of GPMs under different temperatures could be estimated by Equation 3

$$h_{\text{eva},T_1} = \frac{\dot{m}_{\text{water},20^\circ\text{C}}}{\dot{m}_{\text{eva},20^\circ\text{C}}} h_{\text{water},T_1} \quad (\text{Equation 3})$$

The calculated parameters and results were given in Table 1 in the manuscript for the case of 1 sun, and Table S1 for the case of 5 sun.

### Preparation of GO-PEI membranes

First, weigh 25 mg graphene oxide powder and add 50 mL deionized water for 30 min ultrasonic treatment to form graphene oxide dispersion solution. Mix the graphene oxide dispersion solution with 10 mg/L polyethyleneimine solution, followed by 15 min ultrasonic treatment. After that, adjust the PH of mixture solution to 8. Subsequently, 50 mg and 100 mg of 1-ethyl-(3-dimethylaminopropyl) carbodiimide hydrochloride (EDC·HCl) were continuously added to the solution at intervals of 30 min under the action of continuous ultrasound. After the completion of ultrasonic treatment, place the mixed solution on the magnetic stirrer, stir it at 800 rpm for 24 h.

### Pretreatment of nylon filter membrane

In order to enhance the cross-linking between the filter membrane and the mixture, the filter membrane is modified with dopamine before vacuum filtration. The process is as follows: first, weigh 0.2 g dopamine, dissolve it in 100 mL deionized water, then weigh 0.2 g Tris into dopamine solution, adjust the solution pH to 8.5, stirring about 10 min, immerse the filter membrane in the solution. Soak for 3 h, take it out, wash it repeatedly in deionized water, and dry it at  $60^\circ\text{C}$  for standby. The concentration of polydopamine on the surface of nylon filter membrane can be adjusted by changing the soaking time and dopamine concentration.

### Characterizations of the GPMs

The absorption spectra of the selective absorber were measured by ultraviolet-visible spectroscopy (UV-3600, Shimadzu) attached with an  $\Phi 60\text{mm}$  integrating sphere. The microscopic structures and water contact angles of the surface of GPMs were characterized by a scanning electron microscope (ThermoFisher Scientific, Quattro S) and a surface tension/contact angle meter (DSA100), respectively. The IR images of water-pumping processes were captured by an IR camera (FLIR-E6390). The Fourier transform infrared spectroscopy (Nicolet iS50) spectra analysis were used to detect the presence of functional groups on the surface of GO and GPMs. To prove that there are three states of water molecules on the membrane surface and in between the GO layers, we measured the Raman spectra (LabRAM HR Evolution) of water molecules on the surface of GPMs. Differential scanning calorimetry (METTLER TOLEDO, DSC3+) experiments were conducted to directly obtain the vaporization energy of pure water and water in the surface of GPMs.